Electronic Supplementary Material

Sulfur-regulated metal-support interaction boosting the hydrogen evolution performance of Ru cluster in seawater at industrial current density

Ranran Tang, Ping Yan, Yitong Zhou and Xin-Yao Yu**

Experiment Method

Materials

Cadmium nitrate, dopamine hydrochloride, Ruthenium (III) chloride hydrate, Deuterium oxide and Tris (hydroxymethyl) aminoethane were purchased from Shanghai Macklin Biochemical Technology Co., Ltd. Thiourea, potassium hydroxide, tetraethyl silicate, and hydrofluoric acid were obtained from Sinopharm Chemical Reagent Co., Ltd (China). Commercial Pt/C, RuO_2, and Nafion were purchased from Sigma-Aldrich. Seawater was taken from real seawater in Qingdao, Shandong Province, China. The deionized water (DIW, 18.25 M Ω cm^{-1}) used in the experiment was self-prepared. Different concentrations of alkaline simulated seawater (0.5, 1 and 2 M NaCl) electrolytes were prepared by putting different amounts of NaCl solids into 1 M KOH electrolyte. 2.92, 5.84 and 11.68 g of NaCl solids were added into 1 M KOH electrolyte and stirred well to obtained 1 M KOH + 0.5 M NaCl, 1 M KOH + 1 M NaCl and 1 M KOH + 2 M NaCl, respectively. The seawater used in this work was purchased from Qingdao, China and consisted mainly of NaCl, $MgCl_2$, $MgSO_4$, and K_2SO_4. The KOH solids were mixed with real seawater and the pH of the solution was adjusted to 14. After preliminary precipitation, most of the visible particles of precipitates were filtered out and the final clarified solution was obtained as the alkaline real seawater electrolyte which can be directly used for electrocatalytic performance testing.

Synthesis of CdS spheres

2.16 g of $Cd(NO_3)_2{\cdot}3H_2O$, 0.266 g of thiourea, and 0.389 g of PVP were dissolved

in 70 mL ethylene glycol, and stirred vigorously until homogeneous. Subsequently, the mixture solution was sealed in a 100 mL PTFE-lined stainless-steel autoclave and heated at 140 ℃ for 8 h. The mixture solution was centrifugated and washed three times with the ethanol and DIW, respectively, and further dried at 60 ℃ for 12 h.

Synthesis of CdS@PDA spheres

120 mg of CdS spheres were first dispersed into a Tris-buffer solution (pH=8.5) with vigorously stirred for 30 min until a yellow homogeneous solution was obtained. Subsequently, 60 mg of dopamine was added to the above solution and continued to stir at room temperature for 24 h. The mixture solution was centrifugated and washed three times with the ethanol and DIW, respectively.

Synthesis of Ru/SNC spheres

500 mg of CdS@PDA spheres were placed in a tubular furnace and heated to 1000 ℃ in N_2 atmosphere for 3 h. After cooling to room temperature, sulfur and nitrogen co-doped carbon (SNC) hollow spheres were obtained. Next, 20 mg of the obtained SNC spheres were dispersed in 15 mL of DIW with vigorously stirring to a uniform solution. Then, 350 μL $RuCl_3 \cdot xH_2O$ solution (10 mg mL^{-1}) was added to the former solution, stirring again for 4 h. After the reaction, the Ru/SNC product was obtained. The preparation process of Ru_1/SNC and Ru_2/SNC spheres is basically the same as that of Ru/SNC, except for the adjustment of the input of $RuCl_3 \cdot xH_2O$. The amount of $RuCl_3 \cdot xH_2O$ added during the synthesis of Ru_1/SNC spheres was 150 μL and that of Ru_2/SNC spheres was 550 μL. Moreover, the synthesis procedure for Ru/S_1NC and Ru/S_2NC spheres with different S doping amounts was essentially identical to that of Ru/SNC, except for adjusting the weight ratio of CdS to dopamine hydrochloride during the PDA coating step. The weight ratio of CdS to dopamine hydrochloride was adjusted to be 5:2 during the synthesis of Ru/S_1NC spheres, while the weight ratio of CdS to dopamine hydrochloride was modified to be 1:1 during the synthesis of Ru/S_2NC spheres.

Synthesis of SiO_2 spheres

In a typical synthesis, 50 mL of ethanol and 24 mL of ammonia were first

quantified and mixed evenly under stirring. Then, 4.2 mL of tetraethyl orthosilicate was rapidly added to the above solution and continuously stirred at 40 ℃ for 1 h. The products were collected by centrifugation at 5000 rpm for 5 min, washed with ethanol for several times, and dried at 60 ℃ for 24 h.

Synthesis of SiO_2@PDA spheres

First, 100 mg of SiO_2 spheres were dispersed in 100 mL of tris buffer solution and the mixture was ultrasonicated for 30 min to obtain a homogeneous white mixed solution. Then, 60 mg of dopamine hydrochloride was added to the above mixed solution and continuously stirred for 24 h. After reaction, the SiO_2@PDA spheres were obtained after centrifugal washing with DIW and ethanol for three times.

Synthesis of Ru/NC spheres

SiO_2@PDA spheres were placed in a tube furnace and heated to 1000 ℃ in N_2 atmosphere for 3 h. After cooling to room temperature, the obtained black power was named as nitrogen doped carbon sphere. Then, 150 mg of the obtained black powder was added into 45 mL of 5% HF solution and stirred for 10 min. After centrifugation and washing with DIW solution to neutral, nitrogen-doped carbon (NC) hollow spheres were obtained. 20 mg of NC spheres were then dispersed into 15 ml DIW and stirred for 30 min until homogeneous. Then, 0.35 μL of $RuCl_3 \cdot xH_2O$ solution (10 mg mL^{-1}) was added into the above solution and continuously stirred for 4 h. Finally, the Ru/NC spheres were obtained.

Structural Characterizations

The morphology and structure of the materials were characterized by field emission scanning electron microscope (SEM, regulus 8230) and transmission electron microscope (TEM, and HRTEM, JEM-2100F). The aberration corrected high-angle annular dark-field scanning transmission electron microscopy (AC-HAADF-STEM) images were obtained on FEI Titan3 G2 60-300 equipped with a dual aberration corrector at 220 kV. The crystal phase of the samples were analyzed by X-ray diffraction (XRD) on a Bruker AXS GmbH diffractometer. The composition and valence states of the elements on the surface of the samples were investigated by X-ray photoelectron

spectrometer (XPS, ESCALAB 250xi). Thermogravimetric analysis (TGA) was evaluated by TGA 5500 (TA Instruments). Raman and in situ Raman analysis was tested on In Via (Renishaw, UK) using a 532 nm laser. The C, N, and S contents in the samples were measured by Elementar vario EL cube.

Electrochemical Measurements

All electrochemical measurements of the samples were measured with a standard three-electrode setup using a CHI electrochemical workstation (CHI Instruments 760E, China) in 1.0 M KOH and alkaline seawater media. Hg/HgO and graphite rod were used as the reference and counter electrodes, respectively. The catalysts powder was dropped onto a glassy carbon electrode (GCE) (d = 5 mm) as the working electrode. The catalyst ink was prepared by homogeneously dispersing 5 mg of the prepared catalysts and 30 μL of 5 wt% Nafion in a mixture solution (270 μL of ethanol and 200 μL of DIW) under ultrasonication for 1 h. Then, 8 μL of the prepared catalyst ink was dropped onto the GCE. All the potentials were calibrated relative to the hydrogen electrode (RHE) by the Nernst equation of $E_{vs.\ \mathrm{RHE}} = E_{vs.\ \mathrm{Hg/HgO}} + 0.059\ \mathrm{pH} + 0.098$ V. The linear sweep voltammetry (LSV) tests were conducted at a scan rate of 2 mV s^{-1}. 85% iR compensation was used. The electrochemical impendence spectroscopy (EIS) tests were conducted at an amplitude of 5 mV within the frequency range from 0.01 to 10^5 Hz. During the in-situ EIS test, the test potentials were sequenced from low to high overpotentials. The electrochemical double layer capacitance (C_{dl}) was acquired with typical cyclic voltammetry (CV) measurements at different scan rates from 20 to 120 mV s^{-1}. The C_{dl} value was obtained by plotting the $\triangle j(j_a\text{-}j_c)$ in a certain potential versus the scan rate and the slope of the fitting line was half of the C_{dl}. The ECSA of the catalysts was determined by the C_{dl}. The Faradic efficiency (FE) was quantified as the proportion of hydrogen measured experimentally using gas chromatography (GC-9790), relative to the theoretically predicted amount. The FE of H_2 is calculated by the following equation:

$$\mathrm{FE}(\mathrm{H_2}) = \frac{2 \times \mathrm{N} \times \mathrm{F}}{\mathrm{I} \times \mathrm{t}}$$

Where n references the molar amount of produced hydrogen, I stands for the

current during HER, and *t* means the reaction time.

The turnover frequency (TOF) values were calculated by the follow equation:

$$\mathrm{TOF} = \frac{\mathrm{I}}{2 \times \mathrm{N} \times \mathrm{F}}$$

Where *I* is the current (A) during the LSV test, the factor 1/2 takes into the factor that two protons are needed to form a hydrogen molecule with two electrons, *N* is the total number active sites, and *F* is Faraday constant (96485 C mol^{-1}).

KOH/H_2O and KOD/D_2O were used as electrolytes and independently tested for the rate constants K_H and K_D in each solution. The value of KIE was obtained by calculating the ratio of K_H and K_D.

In situ Raman spectroscopy data was collected by an instrument model In Via (Renishaw, UK) with a laser wavelength of 532 nm and a data acquisition duration of 20 s. The Ru/SNC and Ru/NC inks were drop-coated onto NF substrates as working electrodes for in situ Raman tests. Hg/HgO and carbon rods were used as reference and counter electrodes, respectively. 1 M KOH was used as the electrolyte. The Raman cell was sealed during the testing process. The electrochemical workstation applied a constant voltage signal to the working electrode. Raman spectra were first obtained at open circuit voltage, followed by sequential testing from low to high overpotentials to acquire Raman spectra in real time. Each overpotentials was maintained for 5 min and data collection began after 300 s. To avoid chance errors and bubble interference, the Raman test was repeated three times at the same potential.

Assembly and Test of Electrolyzer

The electrolyzer consists of two stainless steel end plates on which a serpentine channel with an area of 1 cm^2 is machined. The prepared Ru/SNC spheres and commercial RuO_2 inks were dripped on the nickel foam (NF) with an area of 1*1cm^2, and the catalyst loading was 1 mg cm^{-2}. After natural drying, they were used as the cathode and anode, respectively. Before test, the cathode and anode were activated by CV method in the electrolyte (1 M KOH/alkaline real seawater) for 30 times. The positive and negative electrodes were separated by anion exchange membrane (FAA-3-PK-130, FuMA-Tech, Germany). The electrolyte was heated in a water bath and

pumped (1 M KOH/alkaline real seawater) through the electrode channel at a speed of 20 mL min^{-1} by a peristaltic pump. The polarization curves and stability of the electrolyzer were tested using the CORRTEST electrochemical workstation.

Theoretical Calculations

Density functional theory (DFT) calculations were carried out using the Vienna ab initio Simulation Package (VASP ver. 6.3.1)[1-3]. The interactions between electronics and ions were described using the projector augmented wave (PAW) method[4]. The exchange and correlation energies were determined with the Perdew, Burke, and Ernzerhof (PBE) functional within the generalized gradient approximation (GGA)[5]. To accurately describe the dispersion interaction, we use DFT-D3 method with Becke-Jonson damping for dispersion correction[6]. A $4\sqrt{3}\times4\sqrt{3}$ supercell of single layer graphite and a Ru cluster with 13 atoms were used to build the calculation model, and an additional vacuum layer of 20 Å was added to the model to avoid the artificial interaction effect between the slab and their mirror images. According to our experimental data, the corresponding proportion of C atoms were replaced by N or S atoms for building Ru/NC and Ru/SNC models. The Brillouin zone sampling was performed on meshes with a *k*-point spacing of 0.05 $Å^{-1}$. The energy criterion was set to 10^{-4} eV in iterative solution of the Kohn-Sham equation. A thermal smearing of 0.05 eV to the orbital occupation was applied to speed up electronic convergence. All the geometrical configurations were illustrated with VESTA software[7].

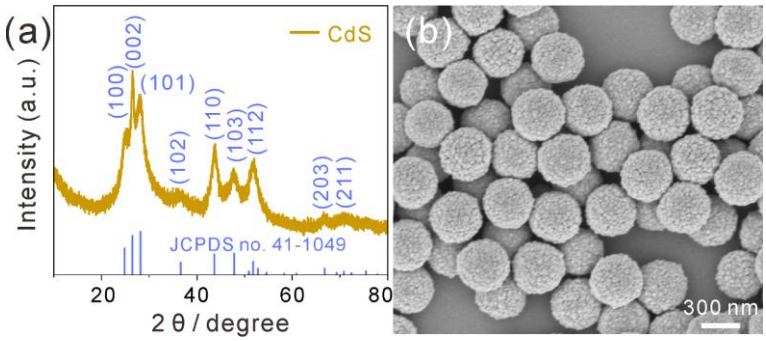

Fig. S1 (a) XRD pattern and (b) SEM image of CdS spheres.

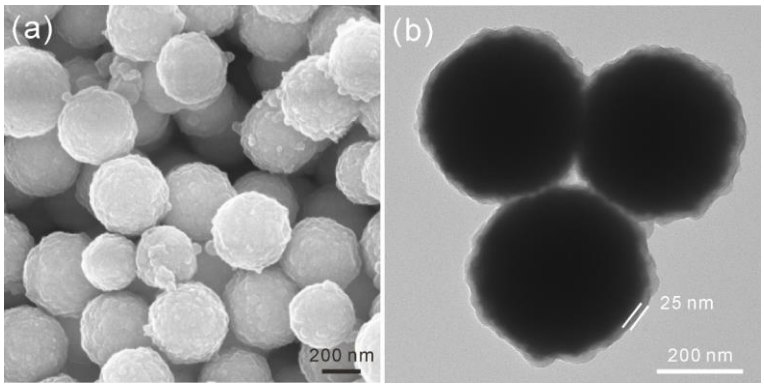

Fig. S2 (a) SEM and (b) TEM images of CdS@PDA spheres.

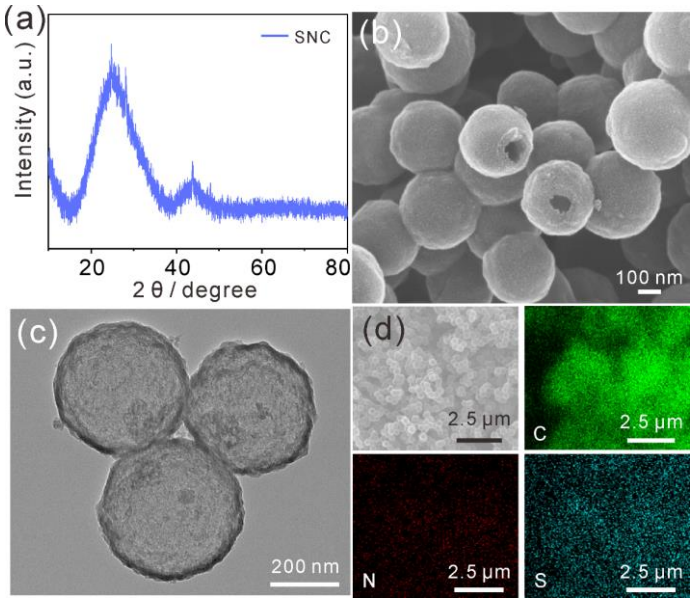

Fig. S3 (a) XRD pattern, (b) SEM image, (c) TEM image, and (d) EDS elemental mapping images of SNC spheres.

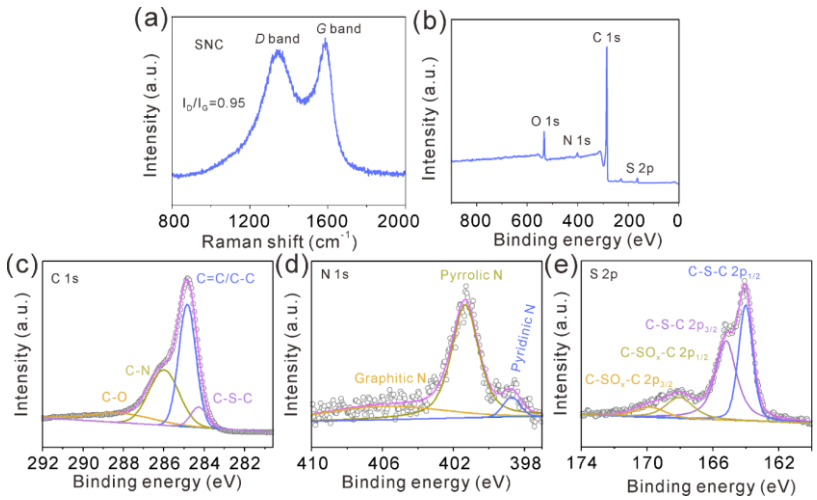

Fig. S4 (a) Raman spectrum of SNC spheres. (b) XPS survey spectrum of SNC spheres. High-resolution XPS spectra of SNC spheres: (c) C 1s, (d) N 1s, and (e) S 2p.

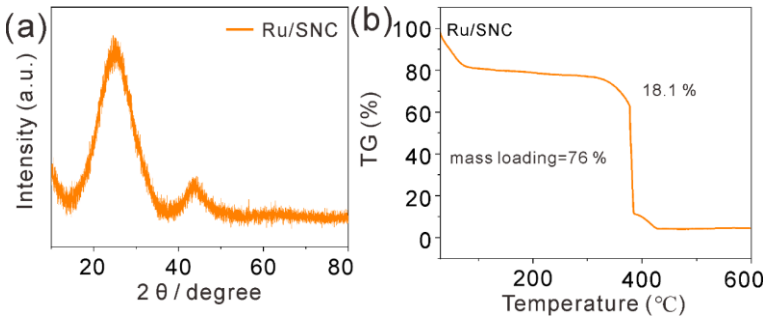

Fig. S5 (a) XRD pattern and (b) TGA curve of Ru/SNC spheres.

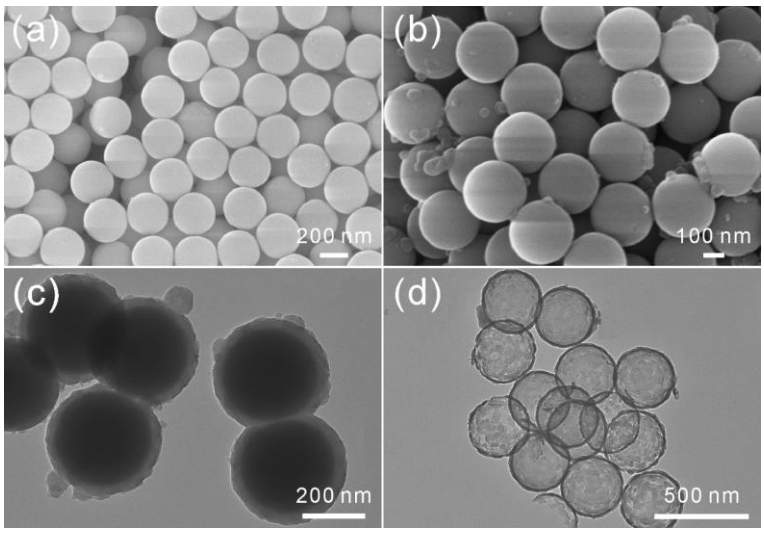

Fig. S6 SEM images of (a) SiO_2, and (b) SiO_2@PDA spheres. TEM images of (c) SiO_2@PDA and (d) NC spheres.

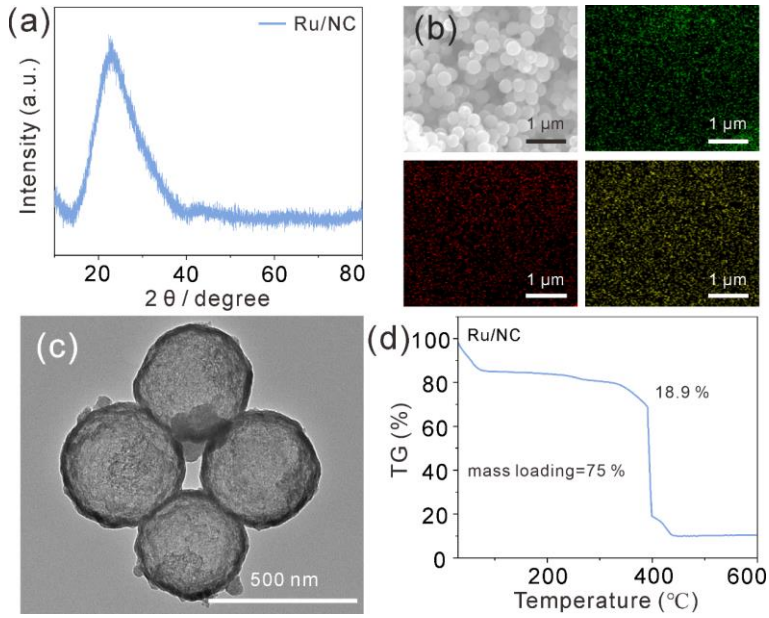

Fig. S7 (a) XRD pattern, (b) EDS elemental mapping images, (c) TEM image, and (d) TGA curve of Ru/NC spheres.

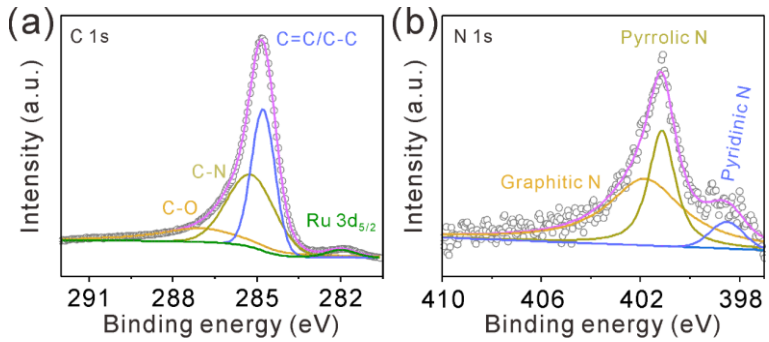

Fig. S8 High-resolution XPS spectra of Ru/NC spheres: (a) C 1s, and (b) N 1s.

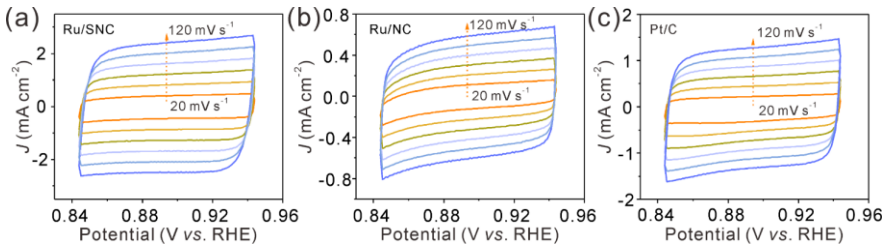

Fig. S9 CV curves of (a) Ru/SNC spheres, (b) Ru/NC spheres, and (c) Pt/C in 1.0 M KOH.

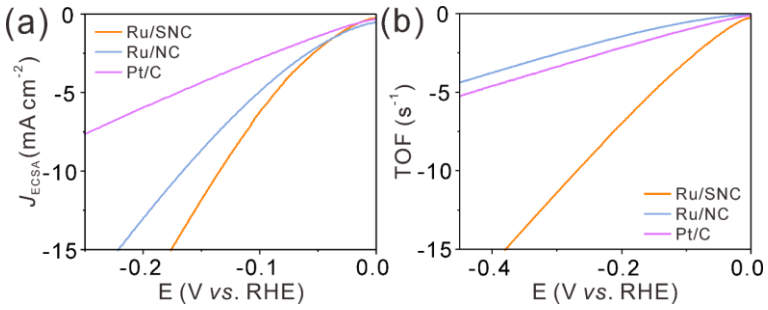

Fig. S10 (a) ECSA-normalized HER polarization curves and (b) TOF curves of Ru/SNC spheres, Ru/NC spheres, and Pt/C.

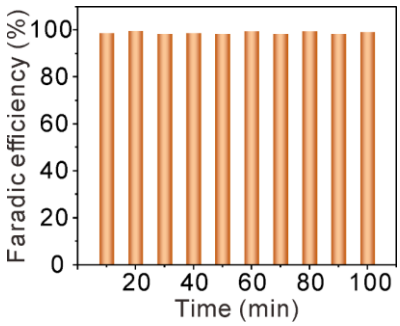

Fig. S11 Faradic efficiency of Ru/SNC spheres at 20 mA cm^{-2} during HER.

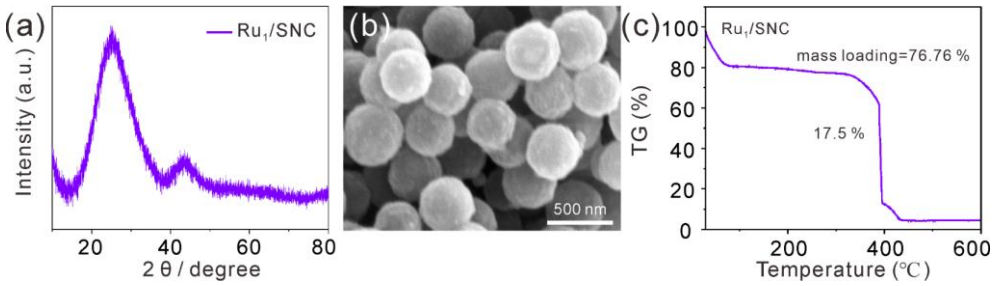

Fig. S12 (a) XRD pattern, (b) SEM image, and (c) TGA curve of Ru_1/SNC spheres.

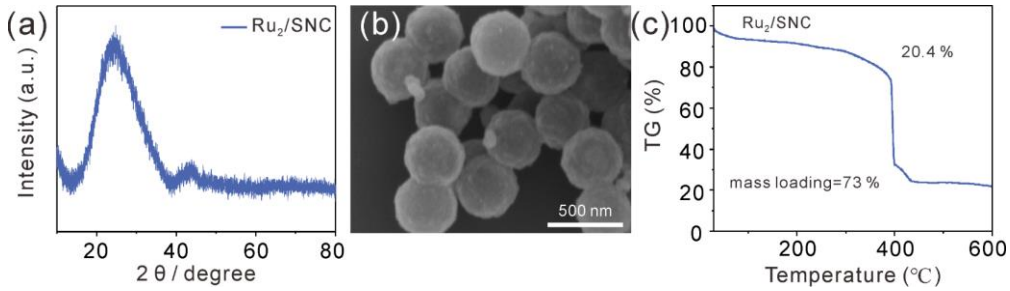

Fig. S13 (a) XRD pattern, (b) SEM image, and (c) TGA curve of Ru_2/SNC spheres.

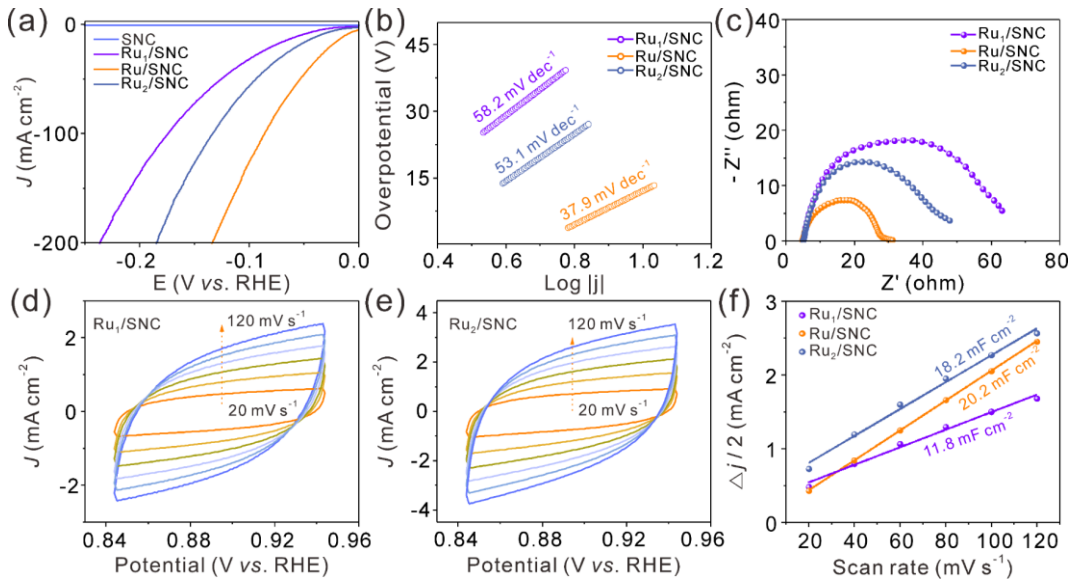

Fig. S14 (a) Polarization curves, (b) Tafel plots, and (c) EIS plots of SNC, Ru_1/SNC, Ru_2/SNC, and Ru/SNC spheres. CV curves at different scan rate from 20 to 120 mV s^{-1} of (d) Ru_1/SNC and (e) Ru_2/SNC spheres. (f) Double electric layer capacitance curve of Ru/SNC, Ru_1/SNC, and Ru_2/SNC spheres.

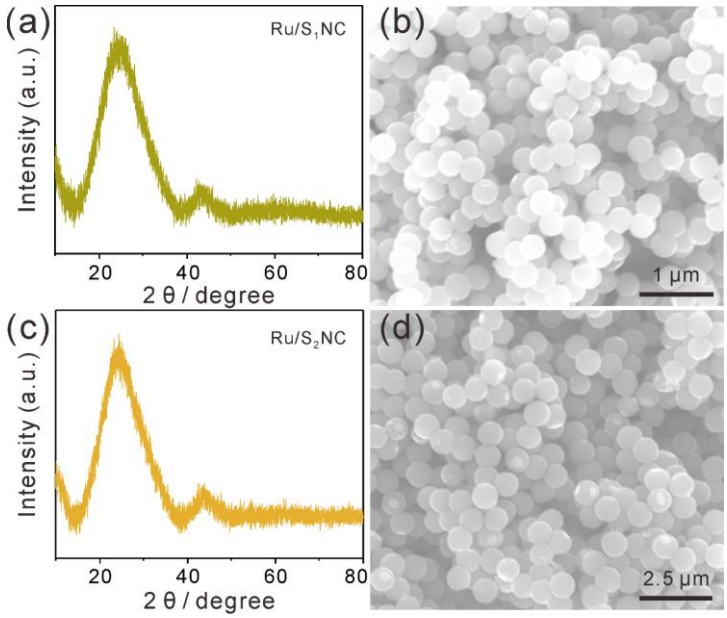

Fig. S15 (a,c) XRD patterns and (b,d) SEM images of Ru/S_1NC (a,b) and Ru/S_2NC (c,d) spheres.

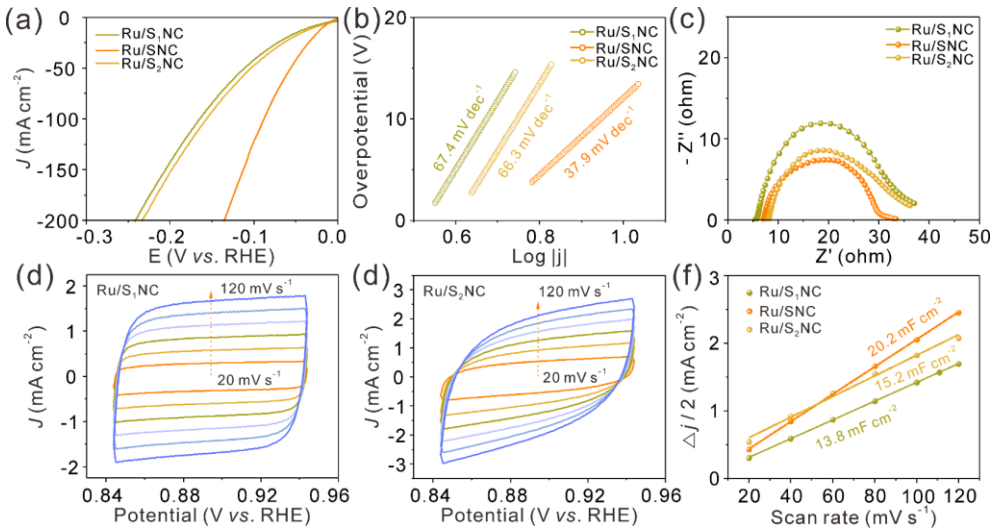

Fig. S16 (a) Polarization curves, (b) Tafel plots, and (c) EIS plots of Ru/S_1NC, Ru/S_2NC, and Ru/SNC spheres. CV curves at different scan rate from 20 to 120 mV s^{-1} of (d) Ru/S_1NC and (e) Ru/S_2NC spheres. (f) Double electric layer capacitance curve of Ru/SNC, Ru/S_1NC, and Ru/S_2NC spheres.

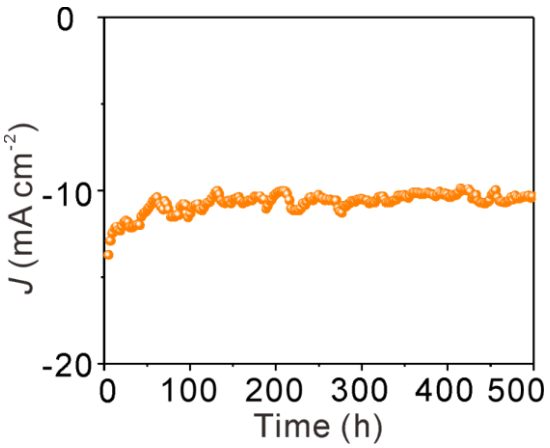

Fig. S17 Stability test of Ru/SNC spheres under the overpotential of 18 mV in 1.0 M KOH.

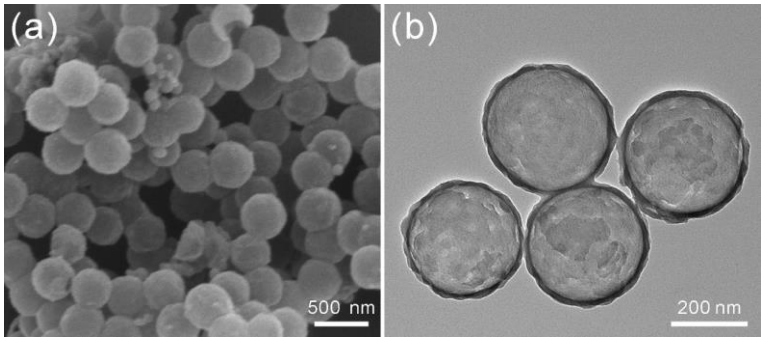

Fig. S18 (a) SEM and (b) TEM images of Ru/SNC spheres after durability test.

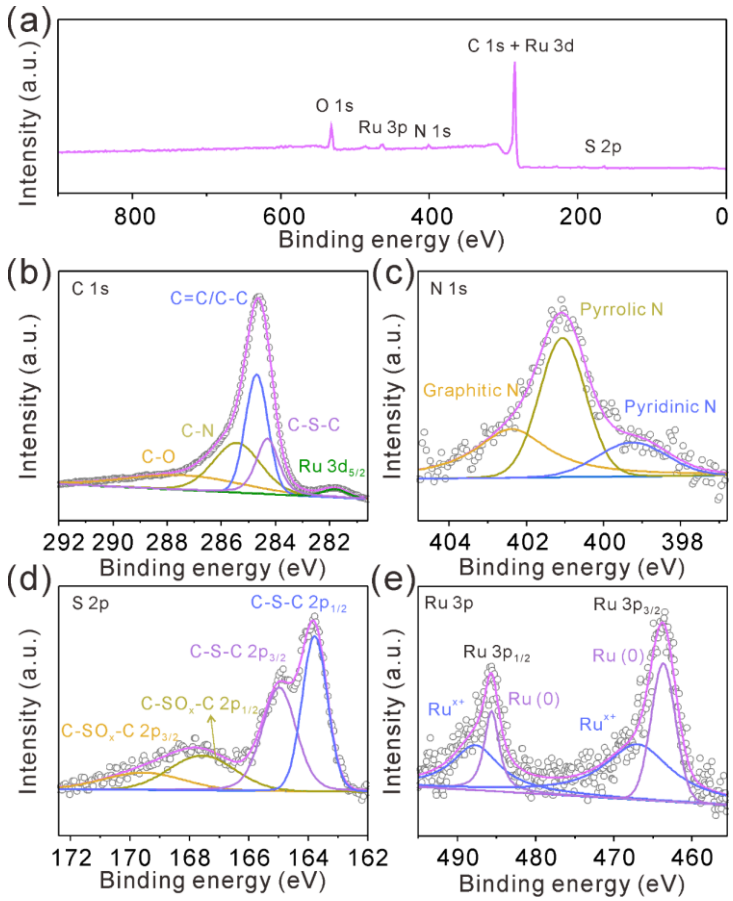

Fig. S19 (a) XPS survey spectra and high-resolution XPS spectra of (b) C 1s, (c) N 1s, (d) S 2p, and (e) Ru 3p of Ru/SNC spheres after stability test in 1 M KOH.

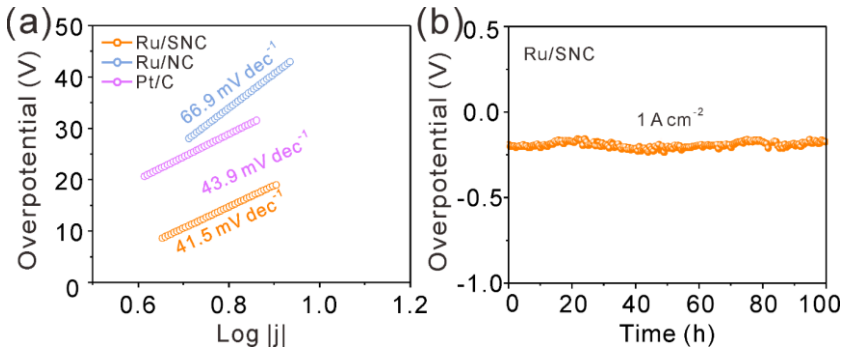

Fig. S20 (a) Tafel plots of Ru/SNC spheres, Ru/NC spheres, and Pt/C, and (b) Stability test of Ru/SNC with a current density of 1A cm^{-2} in alkaline real seawater.

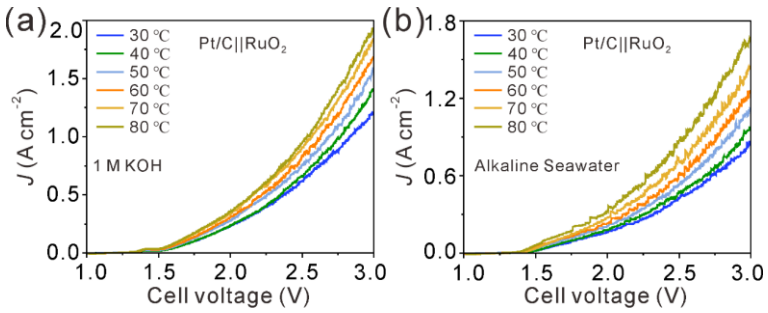

Fig. S21 Polarization curves of Pt/C||RuO_2 at temperature from 30 to 80 ℃ in (a) 1.0 M KOH, and (b) alkaline real seawater.

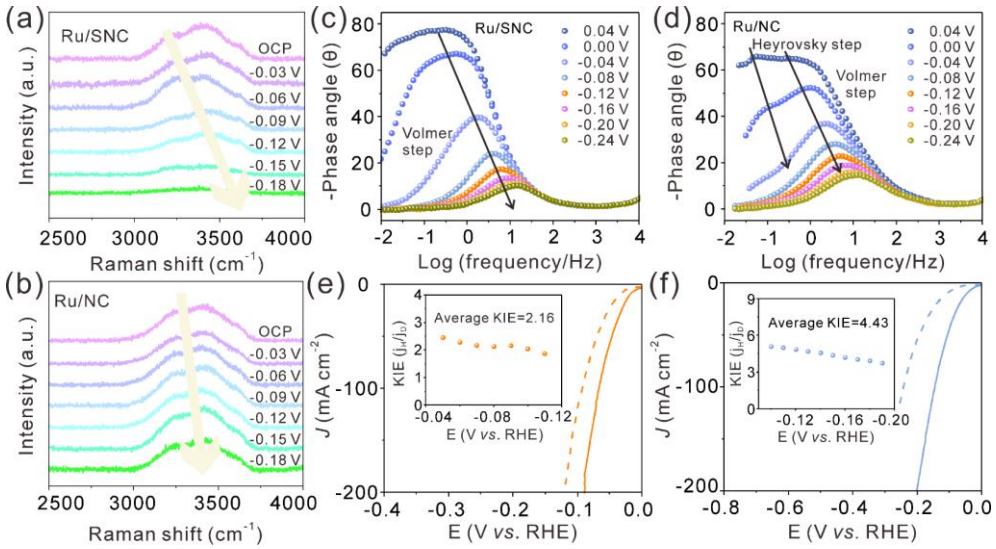

Fig. S22 In situ Raman spectra of (a) Ru/SNC and (b) Ru/NC spheres at different operation potentials from open circuit potential (OCP) to −0.18 V vs. Hg/HgO in 1 M KOH. In situ EIS spectra of (c) Ru/SNC and (d) Ru/NC spheres. The polarization curves and the corresponding KIE value of (e) Ru/SNC and (f) Ru/NC spheres in 1 M KOH/H_2O (solid lines) and 1.0 M KOD/D_2O (dotted lines).

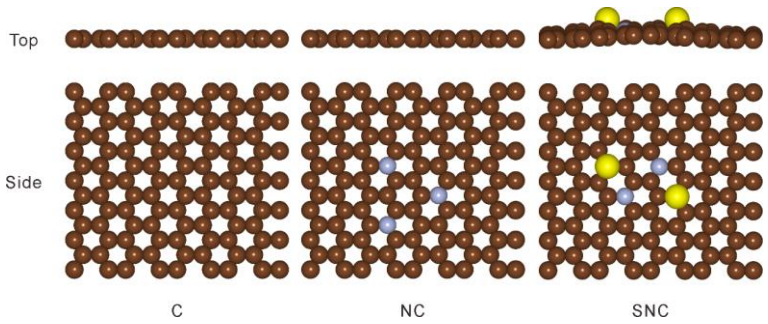

Fig. S23 The optimized atomic structure models of C, NC, and SNC. The dark brown, light blue, and yellow balls represent C, N, and S elements, respectively.

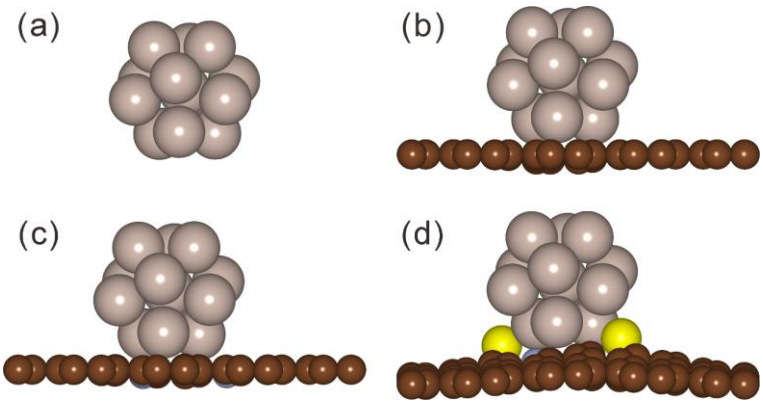

Fig. S24 Atomic structure models of (a) Ru cluster, (b) Ru/C, (c) Ru/NC, and Ru/SNC. The light brown, dark brown, light blue, and yellow balls represent Ru, C, N, and S elements, respectively.

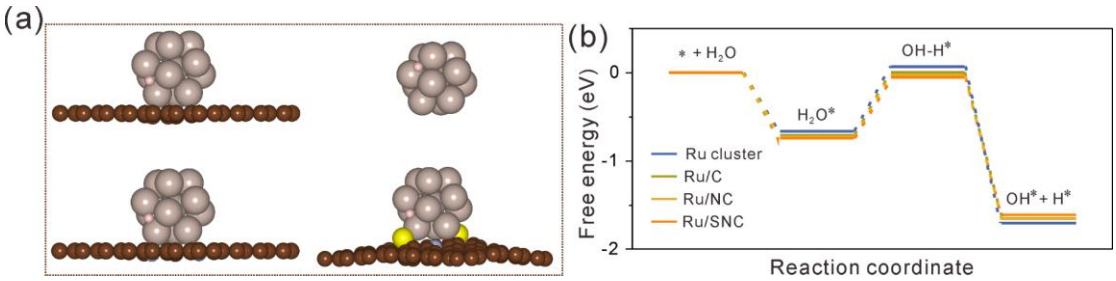

Fig. S25 (a) Geometric configurations of H* adsorption and (b) Gibbs free energy profile for water adsorption/dissociation on Ru/SNC, Ru/NC, Ru/C, and Ru cluster. The light brown, dark brown, light blue, and yellow balls represent Ru, C, N, and S elements, respectively.

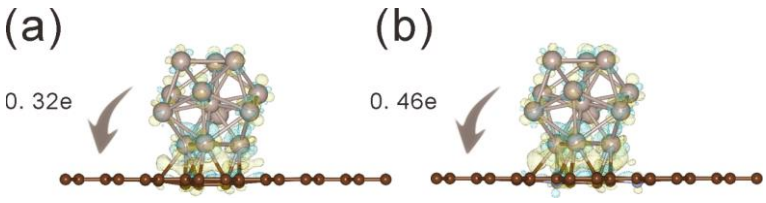

Fig. S26 The charge density difference and Bader charge analysis of (a) Ru/C and (b) Ru/NC. The light brown, dark brown, light blue, and yellow balls represent Ru, C, N, and S elements, respectively.

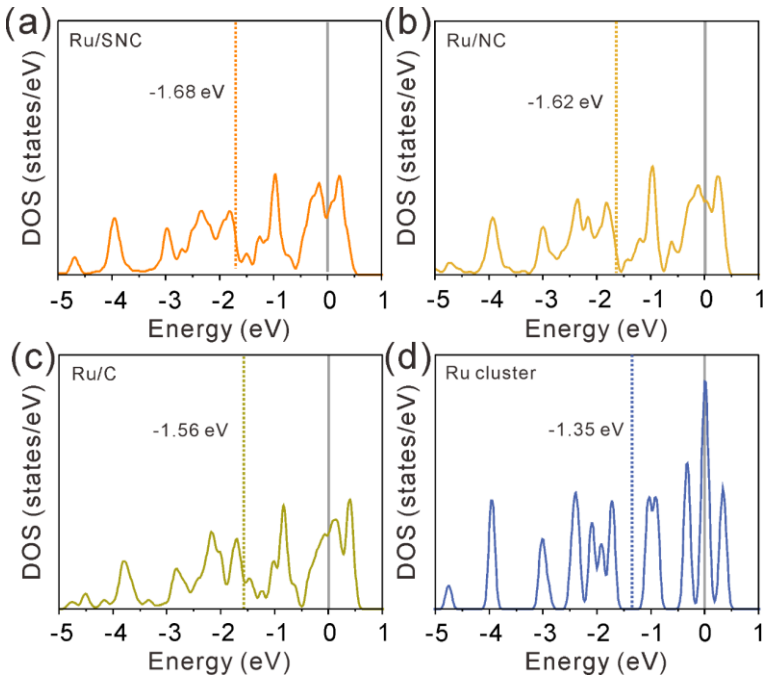

Fig. S27 DOS plots of (a) Ru/SNC, (b) Ru/NC, (c) Ru/C, and (d) Ru cluster.

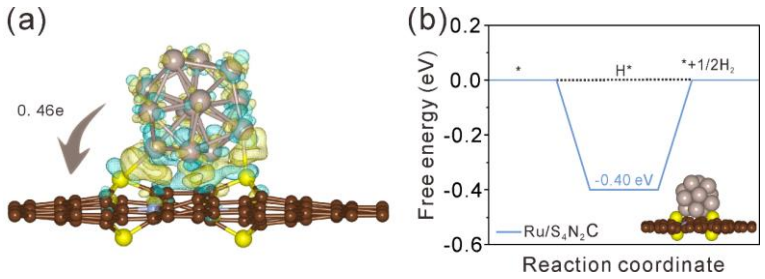

Fig. S28 (a)The charge density difference and Bader charge analysis of Ru/S_4N_2C, and (b) Gibbs free energy diagram for hydrogen adsorption on Ru/S_4N_2C, Inset is the atomic structure models of Ru/S_4N_2C.

Table S1. Elemental analysis results of the prepared samples.

Catalysts	C (wt.%)	N (wt.%)	S (wt.%)
Ru/S_1NC	74.81	2.56	3.88
Ru/SNC	73.94	1.98	4.53
Ru/S_2NC	72.23	1.16	5.33

Table S2. Comparison of HER electrocatalytic activities of Ru/SNC spheres with that of Ru-based catalysts in alkaline solutions reported in recent years.

Catalysts	Electrolyte	η (mV) at 10 mA cm^{-2}	Reference
Ru/SNC	**1 M KOH**	**12**	**This work**
(Ru-Co)O_x-CC	1 M KOH	44.1	[8]
Ru_1CoP/CDs	1 M KOH	51	[9]
$NiRu_{0.13}$-BDC	1 M KOH	34	[10]
Ru-MNSs	1 M KOH	24	[11]
Ru-Ru_2PΦNPC	1 M KOH	46	[12]
Ru@Ni-MOF	1 M KOH	22	[13]
RuCoP	1 M KOH	23	[14]
Ru-CoV-LDH/NF	1 M KOH	28	[15]
Ru@SC-CDs	1 M KOH	29	[15]
Ru/np-MoS_2	1 M KOH	30	[16]
$RuRh_2$	1 M KOH	24	[17]
Ru, W-$NiSe_2$	1 M KOH	100	[18]
Vo-Ru/HfO_2-OP	1 M KOH	39	[19]

References

1. D. J. G. Kress, *Phys. Rev. B*, 1999, **59**, 1758.
2. J. F. G. Kresse, *Phys. Rev. B*, 1996, **54**, 11169.
3. J. F. G. Kresse, *Comp. Mater. Sci*, 1996, **6**, 15-50.
4. P. E. Blöchl, *Phys. Rev. B.*, 1994, **50**, 17953.

5. K. B. J. P. Perdew, *Phys., Rev. Lett.*, 1996, **77**, 3865.
6. R. A. Alberty, *J. Biol. Chem.*, 1969, **244**, 3290-3302.
7. F. I. K. Momma, *J. Appl. Crystallogr*, 2011, **44**, 1272.
8. C. Wang and L. Qi, *Angew. Chem., Int. Ed.*, 2020, **59**, 17219-17224.
9. H. Song, M. Wu, Z. Tang, J. S. Tse, B. Yang and S. Lu, *Angew. Chem., Int. Ed.*, 2021, **60**, 7234-7244.
10. Y. Sun, Z. Xue, Q. Liu, Y. Jia, Y. Li, K. Liu, Y. Lin, M. Liu, G. Li and C.-Y. Su, *Nat. Commun.*, 2021, **12**, 1369.
11. J. Zhang, X. Mao, S. Wang, L. Liang, M. Cao, L. Wang, G. Li, Y. Xu and X. Huang, *Angew. Chem., Int. Ed.*, 2022, **61**, e202116867.
12. J. Yu, G. Li, H. Liu, L. Zhao, A. Wang, Z. Liu, H. Li, H. Liu, Y. Hu and W. Zhou, *Adv. Funct. Mater.*, 2019, **29**, 1901154.
13. L. Deng, F. Hu, M. Ma, S.-C. Huang, Y. Xiong, H.-Y. Chen, L. Li and S. Peng, *Angew. Chem., Int. Ed.*, 2021, **60**, 22276-22282.
14. J. Xu, T. Liu, J. Li, B. Li, Y. Liu, B. Zhang, D. Xiong, I. Amorim, W. Li and L. Liu, *Energy Environ. Sci.*, 2018, **11**, 1819-1827.
15. Y. Liu, Y. Yang, Z. Peng, Z. Liu, Z. Chen, L. Shang, S. Lu and T. Zhang, *Nano Energy*, 2019, **65**, 104023.
16. K. Jiang, M. Luo, Z. Liu, M. Peng, D. Chen, Y.-R. Lu, T.-S. Chan, F. M. F. de Groot and Y. Tan, *Nat. Commun.*, 2021, **12**, 1687.
17. X. Mu, J. Gu, F. Feng, Z. Xiao, C. Chen, S. Liu and S. Mu, *Adv. Sci.*, 2021, **8**, 2002341.
18. Y. Dang, G. Wang, X. Li, X. Ma, F. Yue, C. Wang, L. Gao and F. Fu, *Int. J. Hydrogen Energy*, 2023, **48**, 17035-17044.
19. G. Li, H. Jang, S. Liu, Z. Li, M. G. Kim, Q. Qin, X. Liu and J. Cho, *Nat. Commun.*, 2022, **13**, 1270.